Large Trench-Parallel Gravity Variations Predict Seismogenic Behavior in Subduction Zones

Teh-Ru Alex Song* and Mark Simons

We demonstrate that great earthquakes occur predominantly in regions with a strongly negative trench-parallel gravity anomaly (TPGA), whereas regions with strongly positive TPGA are relatively aseismic. These observations suggest that, over time scales up to at least 1 million years, spatial variations of seismogenic behavior within a given subduction zone are stationary and linked to the geological structure of the fore-arc. The correlations we observe are consistent with a model in which spatial variations in frictional properties on the plate interface control trench-parellel variations in fore-arc topography, gravity, and seismogenic behavior.

Studies of profiles of the gravity field taken perpendicular to the strike of subduction zones suggest that trench-normal gravity profiles are predominantly controlled by mantle rheology, slab buoyancy, and interplate shear tractions on the plate interface (*1*–*8*). Under the premise that spatial variations in gravity over the fore-arc serve as a proxy for the long-term state of stress on the plate interface, we investigate TPGAs using global marine gravity grids (*9*, *10*). Large-amplitude, longer wavelength, trench-normal gravity variations can overwhelm smaller amplitude TPGA (Fig. 1A). Therefore, in constructing maps of TPGAs, we subtract an average regional trench-normal gravity profile from the original free-air gravity data (*11*, *12*) (Fig. 1B). For this analysis, we are concerned only with TPGAs over the location of the plate interface where large-thrust earthquakes occur (less than 50-km depth). We hypothesize that the large-amplitude variations in TPGA that we observed [on the order of 40 mGal (1 Gal = 10^{-2} m s^{-2})] correspond to variations in shear tractions on the plate interface (which are in turn dependent on normal tractions and the coefficient of friction) and may affect the seismogenic character of a given subduction zone. To test this hypothesis, we compare our estimates of TPGA with distributed slip models from selected earthquakes, as well as with the epicenters of large earthquakes from the Harvard Centroid Moment Tensor group and from relocated International Seismological Centre (ISC) global catalogs (*13*–*15*).

We first consider the three largest earthquakes of the century: 1960 Chile [moment magnitude (M_w 9.5)], 1964 Alaska (M_w 9.2), and 1952 Kamchatka (M_w 9.0). For the Alaska/Aleutian subduction zone, we find a strong visual correlation between the location of the principal areas experiencing large coseismic slip in the 1964 Alaska earthquake (M_w 9.2) (*16*) and negative TPGA (Fig. 1B). A region of lower coseismic slip between the two high-slip areas correlates with a region of positive TPGA (Fig. 1B). Regions of large coseismic slip, as inferred from distributed slip models of the 1938 Alaska (M_w 8.3), 1957 Aleutian (M_w 8.6), and 1965 Aleutian (M_w 8.7) earthquakes (*17*, *18*), also occur predominantly in regions of negative TPGA. Areas of large coseismic slip during the 1938 earthquake are bounded to the west (the Shumagin segment) and on their up-dip limit by regions of positive TPGA. Similarly, the along-strike extent of the 1960 Chilean earthquake (*19*) is bounded by regions of increasing TPGA (fig. S3A). The Kurile/Kamchatka subduction zone also shows a strong correlation between the location of large earthquakes and negative TPGA, with an obvious gap in the occurrence of large earthquakes corresponding to a 600-km-long region of positive TPGA (fig. S3B). Areas of large coseismic slip during the 1952 Kamchatka earthquake (*20*), however, correspond to both positive and negative TPGA. The spatial distribution of slip shown for these historical events might not be tightly constrained because of a lack of sufficient data [supporting online material (SOM) text].

We rely on global earthquake catalogs to more systematically explore the relation between occurrences of large earthquakes and TPGA over the past century. We estimate the mean TPGA within the fault area for each subduction zone earthquake with $M_w \geq 6.0$ (*11*). We find that the total seismic moment associated with subduction zone earthquakes located on the slab interface is localized to regions of negative TPGA (SOM text and fig. S3). To emphasize the relation between large earthquakes and TPGA, we consider histograms of moment release versus TPGA, using four bins of about equal area of the plate interface. Seismic moment released in one-fourth of the total area with positive TPGA (>40 mGal) accounts for less than 5% of the total moment released in the 20th century, regardless of whether or not we include the three largest earthquakes. Furthermore, the average seismic moment per event for earthquakes occurring in areas with negative TPGA (<−40 mGal) is more than 10 times as large as that for those occurring in areas with large positive TPGA (SOM text). Although great earthquakes occur predominantly in areas with large-amplitude negative TPGA, the reverse relation does not necessarily hold; i.e., not all regions with negative TPGA necessarily experience great earthquakes.

Using the ETOPO-5 (*21*) digital elevation model, we treat bathymetry in the same manner as the gravity field to form the trench-parallel topography anomaly (TPTA) (*11*). Areas with strongly negative TPGA and TPTA (<–750 m) are the most active in terms of both the number of total events and the number of large events ($M_w \geq 7.5$) (Fig. 2B and fig. S7). Corresponding regions with strongly positive TPGA and TPTA (>750 m) are relatively quiescent. Notably, 14% of the area with strongly negative TPGA and TPTA corresponds to 44% of total moment released, whereas equivalent areas with strongly positive TPGA and TPTA represent only 2% of total moment. Seismic moment density (moment per unit area) in areas with strongly negative TPGA and TPTA (Fig. 2B and fig. S7, blue bin) is more than 40 times as much as that occurring in areas with strongly positive TPGA and TPTA (Fig. 2B and fig. S7, red bin).

Geodetic observations of strain accumulation complement inferences based on earthquake locations by constraining the extent of coupling in a given subduction zone. For instance, a Global Positioning System (GPS) array installed in 1994 to investigate strain accumulation in the Shumagin gap and Kodiak Island in the Alaska/Aleutian subduction zone indicates that Kodiak Island, a region of negative TPGA, overlies a strongly coupled segment of the subduction zone (*22*, *23*) with an implied potential for large earthquakes (Fig. 1B). GPS data for the Shumagin gap, a region of positive TPGA, show much less strain accumulation (*24*, *25*), and the gap is inferred to overlie a segment of the subduction zone that is relatively uncoupled.

Fore-arc basins off the Nankai Trough in Japan are known to coincide with the size and spatial extents of areas of major moment

Seismological Laboratory, Division of Geological and Planetary Science, California Institute of Technology, Pasadena, CA 91125, USA.
*To whom correspondence should be addressed. E-mail: alex@gps.caltech.edu

release during great earthquakes (*26*). The Kermadec subduction zone, normally considered to be relatively aseismic, contains a spatially restricted region several hundred kilometers long, which has experienced several large earthquakes (fig. S8A). This seismically active zone occurs within a much broader region of negative TPGA, but more important, as with Nankai, it conforms to a fore-arc basin characterized by a 1.5-km increase in sediment thickness (fig. S8A) (*27*). Such a strong correlation between topographic depressions and the locations of great earthquakes (*28*) is equivalent to the correlation with large-amplitude negative TPTA.

Along-strike variations in the position of the coastline (*29*) relative to the trench can also be considered as a form of TPTA. For instance, models of coseismic slip from the 1995 M_w 8.1 Antofagasta earthquake (*30*) show that the region of notable coseismic slip terminated just south of the Mejillones Peninsula. It remains to be seen whether slip in the seismic gap to the north (last ruptured in 1877) will extend under the peninsula or stop just north of it. Similarly, no large coseismic slip is inferred to have occurred below Cape Muroto during the 1946 Nankai earthquake (*31*), and during the 1960 Chilean earthquake, coseismic slip is inferred to have decreased substantially before reaching the peninsula south of the city of Concepción (fig. S3A) (*19*). The correlation of bathymetric highs with the absence of great earthquakes (*32*) is equivalent to the correlation with large-amplitude positive TPTA.

We find that TPGA and TPTA are positively correlated in most areas, with little area in regions where TPTA and TPGA are uncorrelated (Fig. 2B; fig. S7). This correlation is expected because gravity anomalies are intrinsically tied to topographic variations by a given compensation mechanism. Results from viscous models (*4*, *5*), viscoelastic models (*6*, *7*), and laboratory experiments (*8*) suggest that spatial variations in the magnitude of shear tractions on the plate interface can modulate surface topography and gravity in the fore-arc. In particular, these models indicate that increasing shear tractions on the plate interface induce a decrease in vertical compressive stress, thereby depressing fore-arc topography and gravity. Consistent with these models, we interpret our observations of TPGA and TPTA as indications of variations in shear tractions on the plate interface, with strongly negative TPGA and TPTA associated with relatively high shear tractions, and strongly positive TPGA and TPTA associated with relatively low shear tractions (Fig. 3, left panel). Laboratory studies of the frictional behavior of sliding rock surfaces show that the tendency for stick-slip behavior (i.e., earthquakes) increases with increasing applied shear tractions (Fig. 3, right panel) (*33*), where shear tractions are a function of the applied normal stress on the sliding block and the coefficient of friction on the contact surface. The effective coefficient of friction on the plate interface is sensitive to many factors, including differences in material properties, presence or absence of fluids, seafloor roughness, slab geometry, temperature, and contact time.

Subduction zones have been classified between two end-member groups, Chilean type and Mariana type (*34*), and large-scale inter-arc differences in seismogenic behavior are usually attributed to variations in age and convergence rate of the subducting plate (*35*) and normal tractions on the plate interface (*36*). However, our observed correlations between smaller scale intra-arc variations in TPGA and TPTA and seismogenic behavior suggest that variations in normal tractions within a given subduction zone are probably not the dominant factor. Negative TPGA and TPTA are associated with a reduction in normal tractions, which would on its own reduce the tendency for stick-slip behavior. The observed correlation of negative TPGA and TPTA with the location of great earthquakes suggests that the implied increases in shear

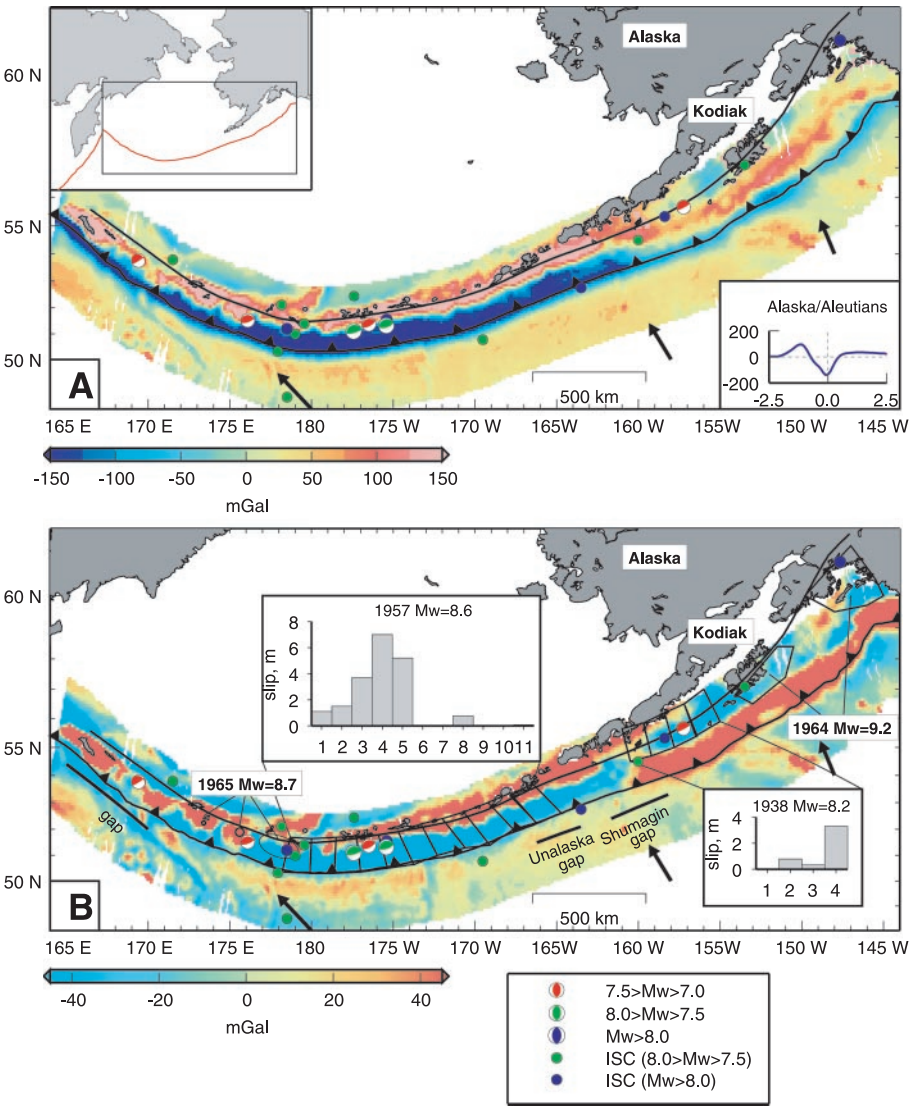

Fig. 1. (**A**) Observed free-air gravity anomaly for the Alaska/Aleutian subduction zone. The average trench-normal gravity profile is calculated for the region shown in the inset and is shown at the lower right, where the horizontal axis shows trench-normal distance in degrees and the vertical axis shows gravity in mGal. The color bar shows the amplitude of the free-air gravity anomaly. (**B**) Estimated TPGA for the Alaska/Aleutian subduction zone. The color bar shows the amplitude of TPGA. For the 1938 and 1957 events (*17*, *18*), we indicate their respective slip distributions in the inset panels, and the fault parameterization is indicated on the TPGA map. Areas with large coseismic slip during the 1964 Alaska and 1965 Aleutian earthquakes (*16*, *17*) are outlined in black lines. For all panels, subduction zone earthquakes from the ISC (1900 to 1976) with $M_w \geq 7.5$ and Harvard CMT (1976 to 2001) catalogs with $M_w \geq 7.0$ are plotted as solid circles and moment tensors, respectively. For both (A) and (B), trench location (*40*) and 50-km slab isodepth contour (*41*) are indicated by the barbed and thick black lines, respectively. Directions of relative plate convergence (*42*) are shown as arrows.

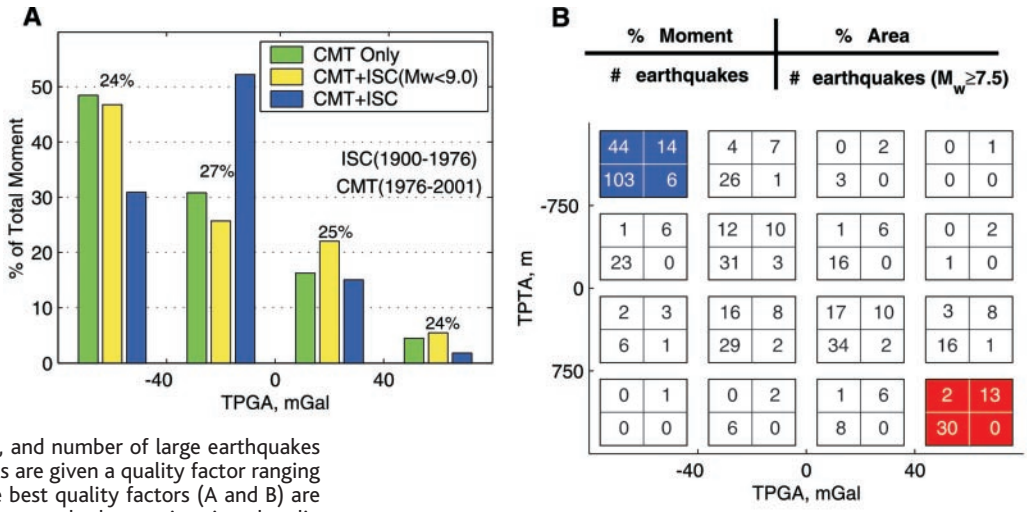

Fig. 2. (**A**) Histogram of total seismic moment versus TPGA. We consider separately events only in the CMT catalog (1976 to 2001), as well as a combined set of CMT (1976 to 2001) and ISC (1900 to 1976). We only considered events with $M_w \geq 6.0$. The percentage of area in each bin is shown above each bar. (**B**) Seismic moment release versus TPGA and TPTA. The number in the upper left of each cell indicates the percentage of total moment associated with the corresponding range of TPGA and TPTA. The numbers at the upper right, lower left, and lower right of each cell indicate the percentage of interface area, number of earthquakes, and number of large earthquakes ($M_w \geq 7.5$), respectively. CMT solutions are given a quality factor ranging from A to H, and only events with the best quality factors (A and B) are considered; a 10-MPa stress drop is assumed when estimating the slip area for each event. Results using all CMT events, a 1-MPa stress drop, or different combinations of catalogs are shown in figs. S4 to S7.

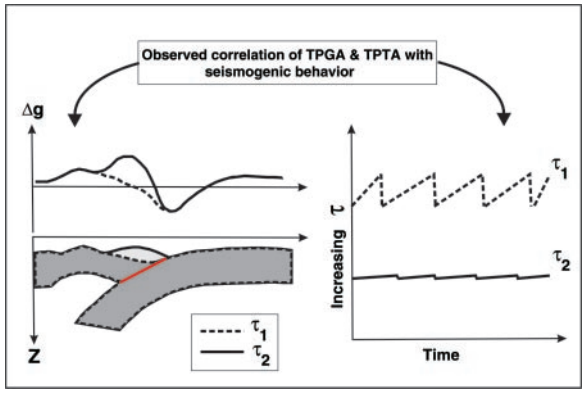

Fig. 3. Illustration of the observed correlation of TPGA and TPTA with seismogenic behavior. The left panel schematically shows variations in gravity and topography due to changes in shear tractions on the plate interface (red line). Solid and dashed lines indicate gravity and topography anomalies corresponding to lower (τ_2) and higher (τ_1) shear tractions on the plate interface. The right panel schematically indicates changes in seismogenic behaviors with changes in shear tractions. Large shear tractions tend to produce stick-slip behavior, and small shear tractions tend to produce stable sliding.

tractions are probably due to increases in the effective coefficient of friction as opposed to decreases in normal tractions. Similarly, positive TPGA, TPTA, and aseismic behavior are associated with relative decreases in the effective coefficient of friction.

On the basis of the observed correlation of TPGA and TPTA with seismogenic behavior, numerical modeling of fore-arc gravity and topography, and laboratory experiments on frictional behavior of sliding surfaces, we conclude that along-strike variations in frictional properties of material on the plate interface within a given subduction zone are as important in controlling seismogenic behavior as are those factors that differ between subduction zones. These variations must be large enough within a given subduction zone to cause a transition between stick-slip and stable sliding behavior.

The amplitude of the variations in gravity and topography addressed here are many orders of magnitude larger than temporal variations over the seismic cycle. Thus, the observed spatial pattern of TPGA and TPTA must persist over time periods much longer than the typical inter-earthquake time (10^2 to 10^3 years) at a given segment of a subduction zone, and great earthquakes should be observed to consistently occur in areas with large-amplitude negative TPGA in the fore-arc region.

On the basis of the observed TPGA, we have made some testable predictions for the seismogenic behavior of different segments of several subduction zones. We predict that the western Shumagin gap, Unalaska gap, and western Aleutians will accumulate elastic strain at shallow depths, whereas the Eastern Shumagin gap, western Aleutians at depths greater than 25 km, and Kurile trench gap should have less strain accumulation (Fig. 1 and fig. S3B). In the northern South American subduction zone, segments between 1°N and 8°S show no occurrences of great earthquakes (*37*). On the basis of the value of TPGA in this region, we predict low elastic strain accumulation in the northern segment (1°N to 3°S) and higher elastic strain accumulation in the southern segment (4°S to 8°S) (fig. S8B). Future geodetic measurements (both on land and on the sea floor) can test our TPGA-based predictions of which seismic gaps are accumulating elastic strain and which are associated with relatively uncoupled plate interfaces (*38*, *39*).

Refining the details of the relation between the gravity field and large earthquakes requires progress in several directions: (i) the simultaneous use of geodetic observations, tsunami waveforms, and seismologic data to determine the absolute location of coseismic slip of large subduction zone earthquakes; (ii) the use of both marine and continental gravity data accounting for sediment thickness and local shallow compensation effects above the plate interface; and (iii) the development of a suite of models investigating the mechanics of the subduction zone process that extend from the time scale of the seismic cycle to millions of years, with attention placed on the long-term topography of the fore-arc.

References and Notes

1. B. H. Hager, R. J. O'Connell, A. Raefsky, *Tectonophysics* **99**, 163 (1983).
2. S. Zhong, M. Gurnis, *J. Geophys. Res.* **99**, 15683 (1994).
3. M. I. Billen, M. Gurnis, *Earth Planet. Sci. Lett.* **193**, 227 (2001).
4. S. Zhong, M. Gurnis, *Geophys. Res. Lett.* **19**, 1891 (1992).
5. S. J. H. Buiter, R. Govers, M. J. R. Worterl, *Geophys. J. Int.* **147**, 415 (2001).
6. S. Wdowinski, *J. Geophys. Res.* **97**, 17651 (1992).
7. R. Cattin, H. Lyon-Caen, J. Chery, *Geophys. Res. Lett.* **24**, 1563 (1997).
8. A. I. Shemenda, in *Subduction: Insights from Physical Modeling*, Modern Approaches in Geophysics, vol. 11 (Kluwer Academic, Dordrecht, Netherlands, 1994).
9. D. T. Sandwell, W. Smith, *J. Geophys. Res.* **102**, 10039 (1997).
10. We restrict ourselves to this global data set to maintain geographic uniformity of the analysis. This restriction implies that we consider only TPGA in offshore areas.
11. Materials and methods are available as supporting material on *Science* Online.
12. The subduction interface can be conveniently classified, using TPGA, into four approximately equal area bins associated with the TPGA ranges of <−40 mGal,

−40 to 0 mGal, 0 to 40 mGal, and >40 mGal, respectively.
13. A. M. Dziewonski, T. A. Chou, J. H. Woodhouse, *J. Geophys. Res.* **86**, 2825 (1981).
14. E. R. Engdahl, D. R. Van der Hilst, R. P. Buland, *Bull. Seismol. Soc. Am.* **88**, 722 (1998).
15. When using these catalogs, we attempt to use only fore-arc thrust events between 0- and 50-km depth in the Benioff zone, where the plate interface is probably coupled.
16. L. Ruff, H. Kanamori, *Phys. Earth Planet. Inter.* **31**, 202 (1983).
17. J. Johnson, *Adv. Geophys.* **29**, 1 (1998).
18. S. Beck, D. H. Christensen, *J. Geophys. Res.* **96**, 2205 (1991).
19. S. E. Barrientos, S. N. Ward, *Geophys. J. Int.* **103**, 589 (1990).
20. J. M. Johnson, K. Satake, *Pure Appl. Geophys.* **154**, 541 (1999).
21. National Geophysical Data Center, ETOPO-5 bathymetry/topography data, *Data Announcement* 88-MCG-02 [National Oceanic and Atmospheric Administration (NOAA), U.S. Department of Commerce, Boulder, CO, 1988].
22. H. J. Fletcher, J. Beavan, J. Freymuller, L. Gilbert, *Geophys. Res. Lett.* **28**, 443 (2001).
23. C. J. Zweck, J. Freymuller, S. C. Cohen, *J. Geophys. Res.* **107**, 10.1029/2001JB000409 (2002).
24. K. M. Larson, M. Lisowski, *Geophys. Res. Lett.* **21**, 489 (1994).
25. J. T. Freymuller, J. Bevan, *Geophys. Res. Lett.* **26**, 3233 (1999).
26. Y. Sugiyama, *Geofis. Int.* **33**, 53 (1994).
27. National Geophysical Data Center, *Total Sediment Thickness of the World's Oceans & Marginal Seas* (NOAA, U.S. Department of Commerce, Boulder, CO, 1996).
28. K. Mogi, *Bull. Earthquake Res. Inst.* **47**, 429 (1969).
29. L. Ruff, B. W. Tichelaar, in *Subduction: Top to Bottom*, AGU Geophysical Monograph Vol. **96**, G. E. Bebout, D. W. Scholl, S. H. Kirby, J. P. Platt, Eds. (American Geophysical Union, Washington, DC, 1996), pp. 105–111.
30. M. E. Pritchard, M. Simons, P. A. Rosen, S. Hensley, F. H. Webb, *Geophys. J. Int.* **150**, 362 (2002)
31. Y. Tonioka, K. Satake, *Earth Planet. Space* **53**, 235 (2001).
32. J. Kelleher, W. McCann, *J. Geophys. Res.* **81**, 4885 (1976).
33. C. Marone, *Ann. Rev. Earth Planet. Sci.* **26**, 643 (1998).
34. S. Uyeda, H. Kanamori, *J. Geophys. Res.* **84**, 1049 (1979).
35. H. Kanamori, *Ann. Rev. Earth Planet. Sci.* **14**, 293 (1986).
36. C. H. Scholz, J. Campos, *J. Geophys. Res.* **100**, 22103 (1995).
37. T. Lay, H. Kanamori, L. Ruff, *Earthquake Pred. Res.* **1**, 1 (1982).
38. S. P. Nishenko, *Pure Appl. Geophys.* **135**, 169 (1991).
39. Y. Y. Kagan, D. Jackson. *J. Geophys. Res.* **100**, 3943 (1995).
40. National Geophysical Data Center, Global Relief data (CD-ROM) (World Data Center for Marine Geology and Geophysics, Boulder, CO, 1993).
41. O. Gudmundsson, M. Sambridge, *J. Geophys. Res.* **103**, 7121 (1998).
42. C. DeMets, R. G. Gordon, D. F. Argus, *Geophys. Res. Lett.* **21**, 2191 (1994).
43. We are grateful for two anonymous reviewers as well as thorough reviews by D. Anderson, M. Billen, M. Gurnis, H. Kanamori, T. Lay, R. Lohman, and J. Polet in earlier versions of this paper. We also thank R. Wells for open and enthusiastic discussions.

Supporting Online Material
www.sciencemag.org/cgi/content/full/301/5633/630/DC1
Materials and Methods
SOM Text
Figs. S1 to S8
References

10 April 2003; accepted 25 June 2003

Extended Boltzmann Kinetic Equation for Turbulent Flows

Hudong Chen,[1] Satheesh Kandasamy,[1] Steven Orszag,[2] Rick Shock,[1] Sauro Succi,[3]* Victor Yakhot[4]

Complex fluid physics can be modeled using an extended kinetic (Boltzmann) equation in a more efficient way than using the continuum Navier-Stokes equations. Here, we explain this method for modeling fluid turbulence and show its effectiveness with the use of a computationally efficient implementation in terms of a discrete or "lattice" Boltzmann equation.

The conventional approach to analyzing continuum physics is to use a coarse-grained model in terms of macroscopic variables. For example, fluid dynamics is usually formulated in terms of the Navier-Stokes equations for the macroscopic velocity and pressure as functions of position $\mathbf{x}$ and time t. In the presence of complex physical effects such as turbulence or multiphase physics, the solution of these basic coarse-grained equations becomes difficult. In such cases, simplified models can be used to modify the underlying coarse-grained equations; one example is the eddy viscous turbulence model. However, models of this sort still cannot reliably reproduce many observed physical effects.

Here, we analyze a different approach based on extensions of the Boltzmann equation (*1*). The premise of this approach is that it is simpler to model complex physics first at the Boltzmann (or kinetic) level, and then use coarse-graining procedures only after modeling is done. We solve the appropriately modeled kinetic equations numerically, and then we average (or project) the dynamical variables to obtain coarse-grained results for macroscopic quantities such as velocity and pressure.

Boltzmann [(*1*), see also (*2*)] expressed the behavior of many-particle kinetic systems in terms of the basic mechanical laws governing single-particle motions at atomic or molecular scales. Boltzmann formulated the problem in terms of the one-body distribution function $f(\mathbf{x},\mathbf{v},t)$, which is the number density of molecules at position $\mathbf{x}$ and speed $\mathbf{v}$ at time t. In the absence of external forces, the resulting Boltzmann equation is

$$\frac{Df}{Dt} \equiv \frac{\partial f}{\partial t} + \mathbf{v} \cdot \frac{\partial f}{\partial \mathbf{x}} = C(f,f) \qquad (1)$$

The left side of this equation represents the free streaming of molecules in space, whereas the right side denotes a complicated integral operator in velocity space expressing intermolecular interactions or collisions. Once the distribution function f is known, macroscopic observables such as fluid density, speed, and pressure are obtained by integration over the molecular velocity degrees of freedom.

Equation 1 provides the mathematical framework to derive evolution equations for the macroscopic variables in the limit of weak departures from local thermodynamic equilibrium (LTE). For example, coarse graining of Eq. 1 [see (*3*)] leads to the macroscopic Navier-Stokes equations for fluid flow (*4*) in terms of the fluid velocity $\mathbf{u}$, pressure p, and kinematic viscosity ν. Equation 1 describes large departures from LTE, as can occur near sharp interfaces. The Navier-Stokes equations are mathematically complex, having resisted most attempts at a solution for more than a century, especially for turbulent flows (*5*–*7*).

In its simplest instance, fluid turbulence is thought to be controlled by a single parameter, the Reynolds number $Re = UL/\nu$, where U is the typical macroscopic speed of a flow, and L is a typical macroscopic scale. When $Re \gg 1$, turbulence occurs and there is an energy cascade from large scales, L, where energy is input to drive the flow, down to small scales (of order $L/Re^{3/4}$) where energy is dissipated (*8*).

In solving turbulent flow problems by direct numerical simulation (DNS), one resolves all these relevant excited degrees of freedom. This is a virtually impossible task when $Re \gg 1$. For example, computation of flow past an automobile at $Re \approx 10^6$ requires at least 10^{14} degrees of freedom, enough to more than saturate the most powerful present-day computers.

High-Re flows must therefore be approximated or modeled using far fewer degrees of freedom. The usual first step in turbulence modeling is to split the turbulent velocity field $\mathbf{u}$ into coarse-grained (slow, large-scale) and fluctuating (fast, small-scale) components, $\mathbf{U}$ and $\mathbf{u}'$, respectively.

[1]EXA Corporation, 450 Bedford Street, Lexington, MA 02420, USA. [2]Department of Mathematics, Yale University, New Haven, CT 06520, USA. [3]Istituto Applicazioni Calcolo, CNR, Viale del Policlinico 137, 00161 Roma, Italy. [4]Department of Aerospace and Mechanical Engineering, Boston University, Boston, MA 02215, USA.

*To whom correspondence should be addressed. E-mail: succi@iac.rm.cnr.it

Supporting Online Material

Materials and Methods

Construction of TPGA

The choice of the along-strike extent of the region used to calculate the local average trench-normal gravity profile is non-unique. Our choice corresponds to the regions outlined in Fig. S1. Each region incorporates at most the entire extent of a given subduction arc, and at a minimum, the rupture zone of several great earthquakes (Fig. 1B, Figs. S2, S3, S8). By construction, the TPGA in a given region will integrate to zero along any path a constant distance from the trench. In general, the gradients of TPGA discussed in this study are visible in the original free air gravity data (compare Figs. 1A and 1B). The removal of the average trench normal profile serves to put all subduction zones on a more comparable footing. The resulting TPGA primarily reflects short wavelength variations in shallow fore-arc structures (Fig. 1B), and can vary strongly in directions both parallel and perpendicular to the strike of the trench. There is no obvious systematic dependence of TPGA on the age of subducting plates or the type of overriding plate (continental or oceanic). We have used different sub-regions to calculate TPGA, and found very similar estimate of TPGA (Fig. S2).

Estimation of TPGA associated with subduction zone earthquakes

Because events in the relocated ISC and Harvard CMT catalogs are treated as point sources, we must assume a relationship between the size of the earthquake and the area that slipped. We assume a dip-slip rectangular fault with dimensions that scale with seismic moment and stress drop (*S1*). We consider extremal values of stress drops in the range of 1-10 MPa (*S2*). The slip area of each event is assumed to be square and centered on the hypocenter. If this assumption results in surpassing the surface or down dip limit of the slab interface, the assumed area becomes rectangular,

with the slipping area extending along strike. The CMT location is determined as the centroid of energy release and considered as the best available global dataset of seismic moment and location. The CMT catalogue we use spans the time period from 1976 to 2001, while the relocated ISC catalogue begins in 1900. For events in the ISC catalogue without a corresponding CMT-determined seismic moment, we estimate moment via a moment-magnitude relationship (*S3, S4*).

The distribution of co-seismic slip for the three largest earthquakes may be complicated and our assumed hypocenter, fault area, and computed mean TPGA, may thus not adequately approximate reality. Therefore, for these three events, we use available distributed slip models (*S5, S6, S7*) to compute their associated TPGA.

Construction of TPTA

As with the TPGA, we bin the TPTA in four groups with equal total area in a given range of TPTA. We note that ETOPO-5 data is not as highly resolved as the gravity data (*S8, S9*). Gravity data is higher solution with 30 sec grid spacing while ETOPO-5 data is with 5 min grid spacing. Track lines used to construct ETOPO-5 are denser in along the convergent plate boundary (refer Fig. 1 in S9,) the error due to griding is not likely to be significant at the scales we are interested (several tens of kilometers).

Supporting Online Text

Moment release vs. TPGA

We first consider the distribution of moment for individual events versus TPGA (Fig. S3). For events in either the CMT or the ISC catalogues, no great earthquakes (Mw≥8.0) occur in areas with positive TPGA (> 40 mGal). Given the large number of events involved, we find it useful to also consider the distribution of cumulative moment (Fig. S4). We observe that about 80% of the cumulative moment is produced in 30% of total area of subduction zone with TPGA less than -30 mGal, while less than 20% of cumulative moment is produced in the 70% of the area of subduction zone with TPGA greater than −30 mGal. The total cumulative seismic moment is dominated by the three largest earthquakes of the 20^{th} century. When excluding the three largest earthquakes, we find that about 45% of the remaining total seismic moment is produced in about 25% of the total area of subduction zone with highly negative TPGA (< -40 mGal).

Robustness of correlation between TPGA and seismic moment

Despite the inherent limitations of the global earthquake catalogues, such as event mislocation and incompleteness, the correlation between TPGA and the occurrences of large earthquakes does not depend on the assumed magnitude of the stress drop, which catalog is used, or how seismic moment is distributed over a given earthquake's fault area (Fig. S5 and Fig. S6). In addition, Monte-Carlo permutation tests (*S10*) indicate that the difference in total seismic moment between areas with strongly negative TPGA (< −40 mGal) and areas with strongly positive TPGA (> 40 mGal) is significant at a 95% confidence level.

Supporting Online Figure S1

Caption Figure S1: Location of the subduction zones considered in this study: **(A)** Alaska-Aleutian **(B)** Kamchatka-Kurile **(C)** Japan **(D)** Nankai **(E)** Ryukyu **(F)** Izubonin-Mariana **(G)** Sumatra-Java **(H)** Tonga-Kermadec **(I)** Chile **(J)**, northern South America, **(K)** Central America and **(L)** Cascadia. Average trench-normal profiles are computed using the regions as outlined.

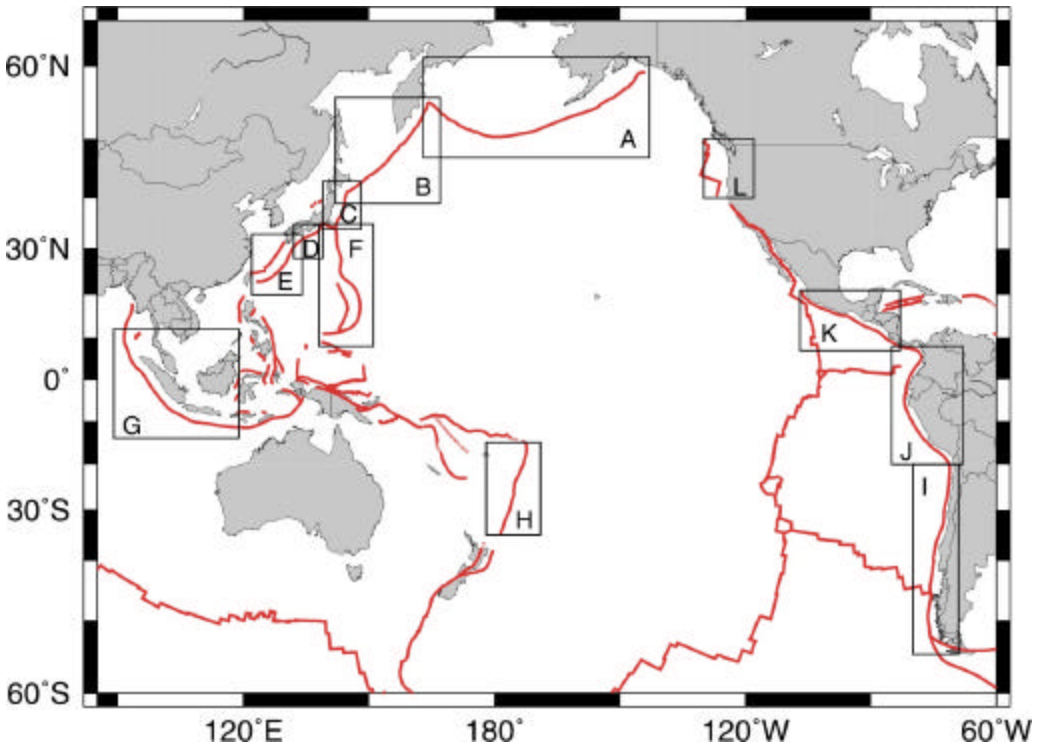

Supporting Online Figure S2

Caption Figure S2: TPGA computed using different sub-regions for **(A)** Alaska **(B)** Aleutian **(C)** Kamchatka **(D)** Kurile, respectively. The average trench-normal gravity profile is calculated for the region shown in the inset and shown in the sub-panel of Fig. 1A. The x-axis is trench-normal distance in degrees and the y-axis is gravity in mGal. The color bar shows the amplitude of the free-air gravity anomaly. subduction zone earthquakes from the ISC (1900-1976) with M_w=7.5 and Harvard CMT (1976-2001) catalogues with M_w=7.0, are plotted as solid circles and moment tensors, respectively. Trench location (*S11*) and 50-km slab iso-depth contour (*S12*) are indicated by the barbed and thick black lines, respectively. Directions of relative plate convergence (*S13*) are shown as arrows.

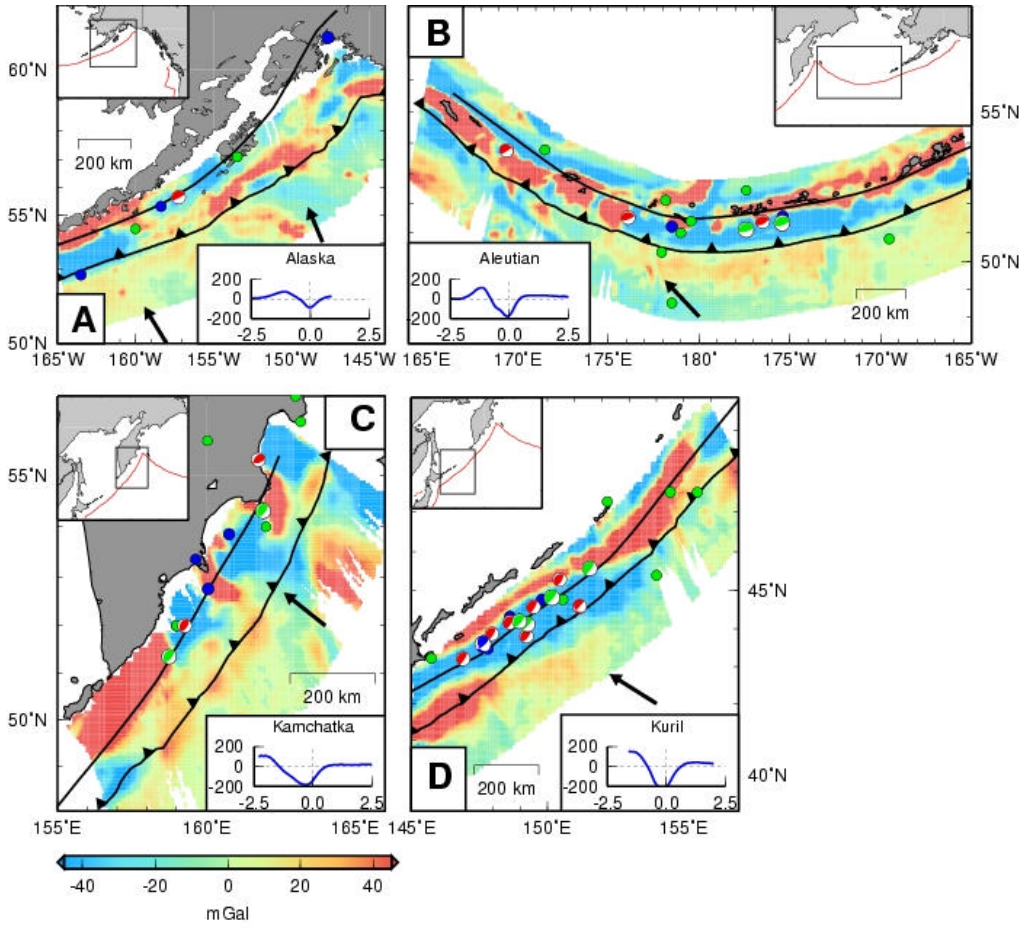

Supporting Online Figure S3

Caption Figure S3: **(A)** Observed TPGA in the Southern Chile subduction zone. Average trench-normal profile is computed in region (I) shown in Fig. S1. Black solid line represents 10 m contour of co-seismic slip of the 1960 Chilean earthquake (*S14*). **(B)** Observed TPGA in Kamchatka-Kurile. Previously documented seismic gap (*S15*) is shown by a black bar. Areas with large moment released during 1952 great earthquakes are indicated in black boxes (*S16*). Symbol descriptions follow Fig. S2.

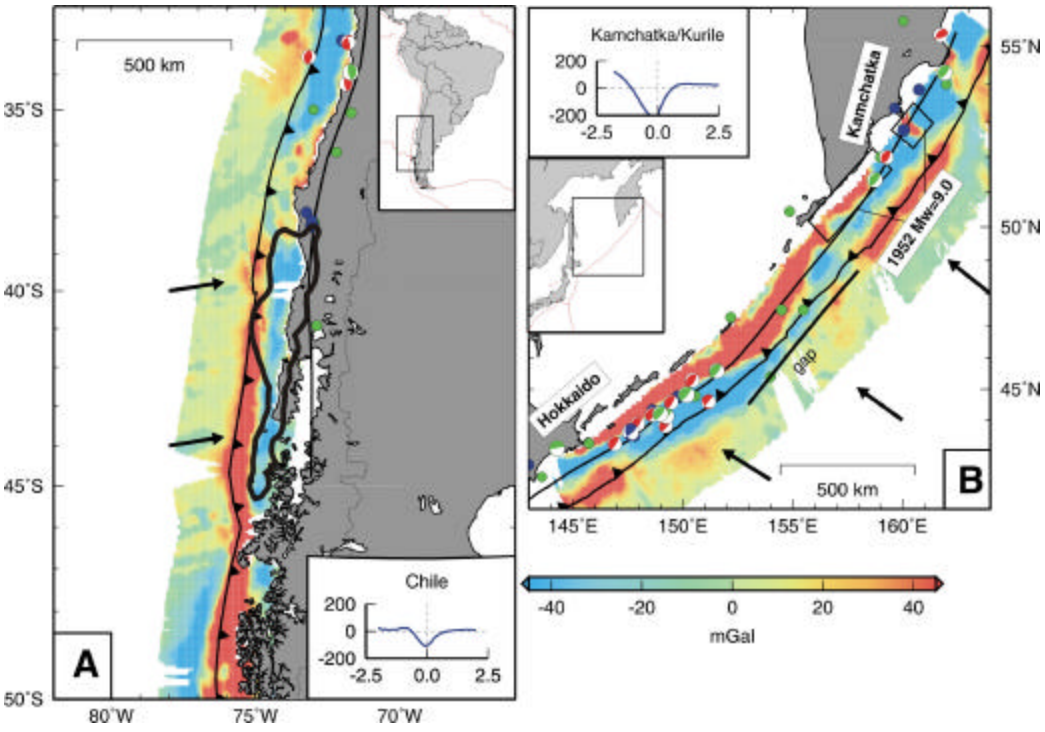

Supporting Online Figure S4

Caption Figure S4: Scatter plot of M_w vs. TPGA. Solid and open circles indicate data from CMT and ISC catalogue, respectively. Cumulative percent of total seismic moment with respect to TPGA for the entire ISC catalogue, ISC catalogue with M_w<9.0, and CMT catalogue are shown with green, red and blue lines, respectively. Mean TPGA for the three giant events are calculated using available slip models (*S14, S16, S17*). Dashed lines indicate the values of TPGA that divide the total area of subduction zone interface into four bins of approximately equal area.

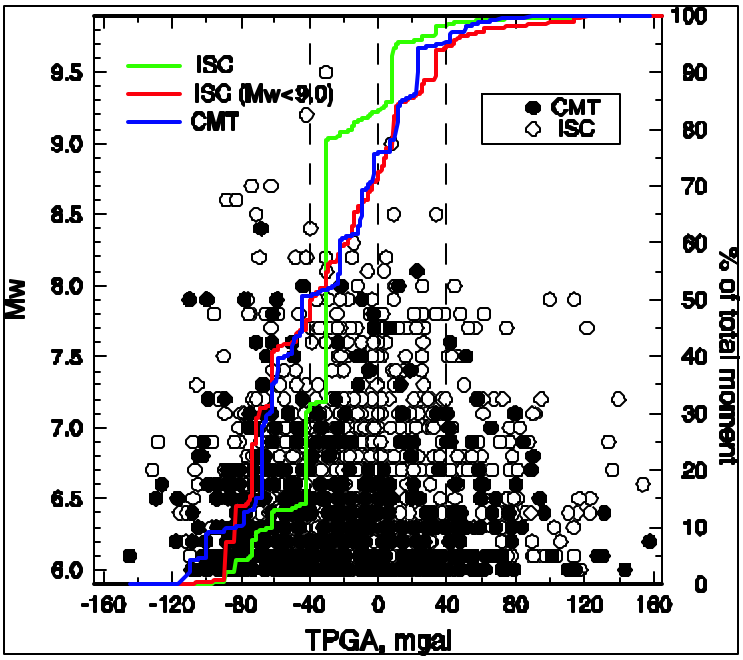

Supporting Online Figure S5

Caption Figure S5: Histogram of total seismic moment vs. TPGA for **(A)** All CMT events (1976-2001) with M_w=6.0. **(B)** All events with M_w=6.0 located in both CMT and ISC catalogues (1976-2001). A 10 MPa stress drop is assumed when estimating slip area. **(C)** All ISC events in 1900-1976. **(D)** All CMT events (1976-2001) and ISC events (1900-1976).

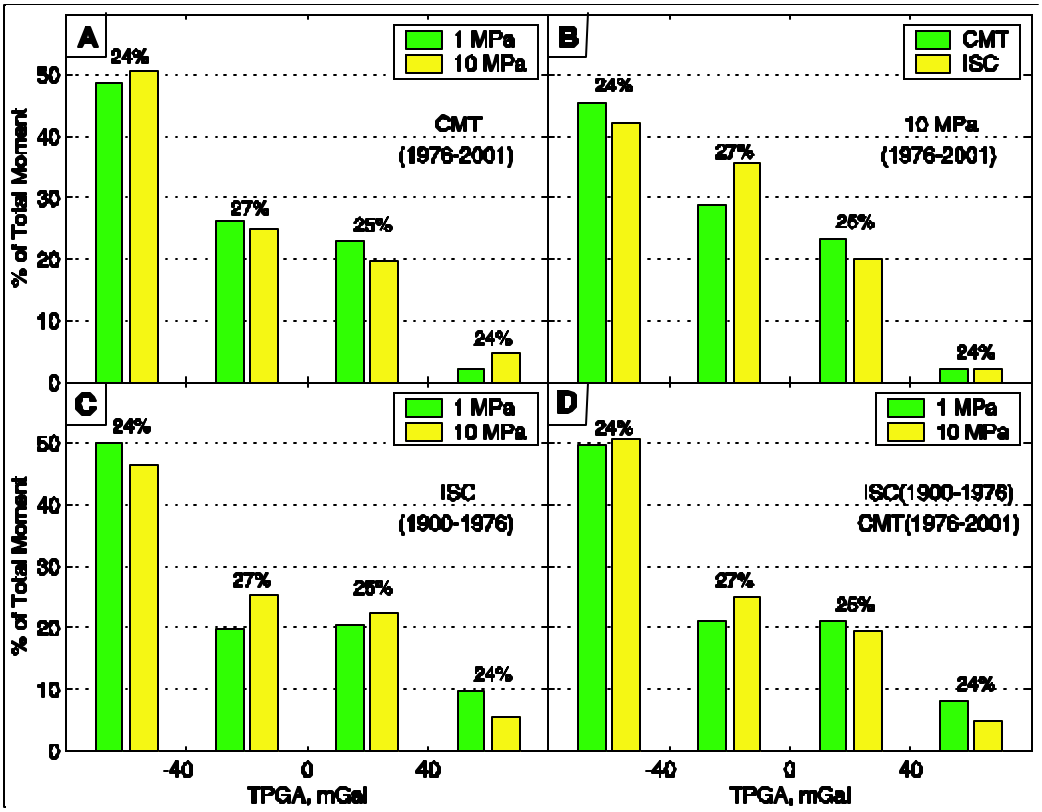

Supporting Online Figure S6

Caption Figure. S6: Histogram of total seismic moment vs. TPGA derived using an alternative approach from that used in all other figures. Here we do not calculate the average TPGA for a given earthquake. Instead, the plate interface is pixilated into small (about 0.1 x 0.1 deg) cells of constant TPGA, and the seismic moment for a given earthquake is evenly distributed onto the cells within the estimated fault area. We then form the histogram by evaluating the total distributed moment in cells lying within a given range of TPGA. **(A)** All CMT events (1976-2001) with M_w=6.0. **(B)** All ISC events from 1900-1976. The percent of the slab interface area represented by each bin is shown above each bar.

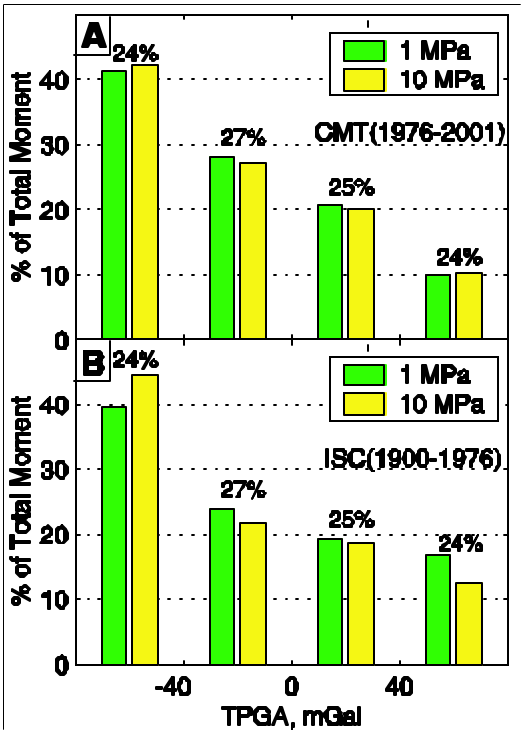

Supporting O nline Figure S7

Caption Figure S7: Seismic moment release vs. TPGA and TPTA using all CMT events with M_w=6.0 assuming a 1 MPa stress drop to calculate the slip area. **(A)** Number of event **(B)** percent of slab interface area **(C)** percent of seismic moment **(D)** Seismic moment density.

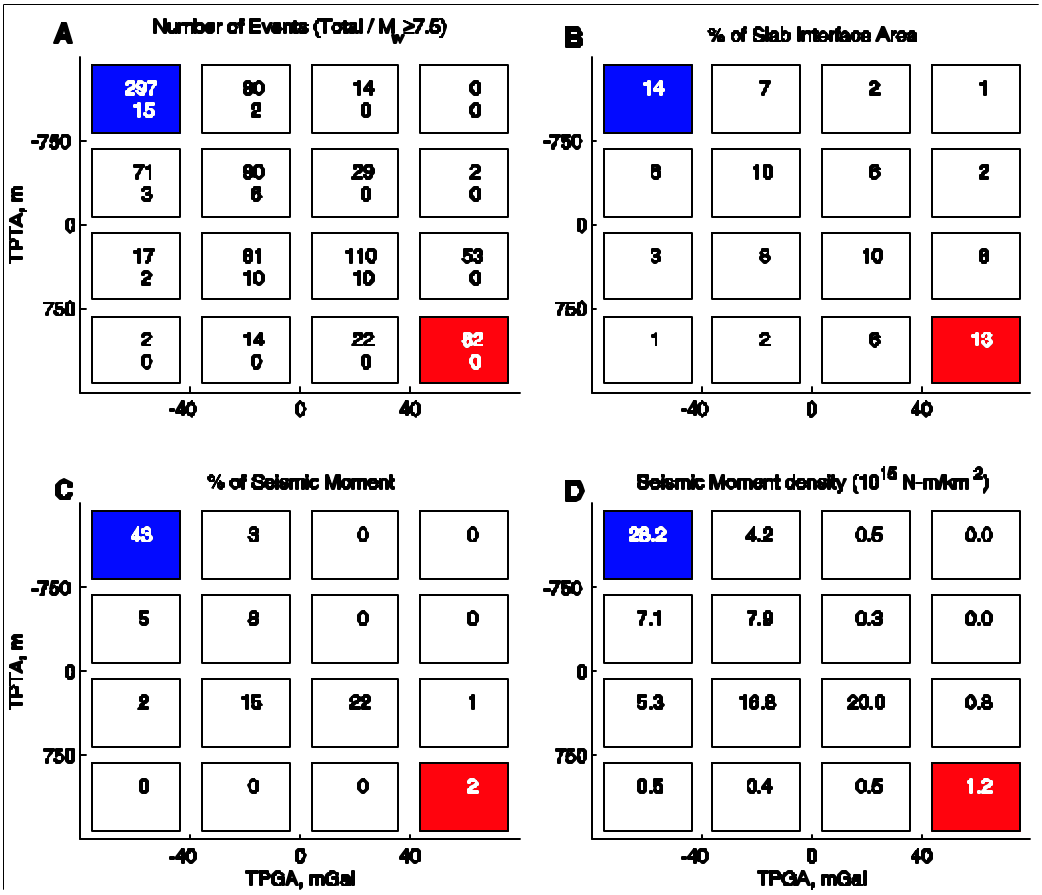

Supporting Online Figure S8

Caption Figure S8: **(A)** Observed TPGA in Kermadec. The average trench-normal profile is computed in region H shown in Fig. S1. Contours indicate sediment thickness (*S18*) in meters. **(B)** Observed TPGA in northern S. America. The extent of previously determined seismic gap (*S15*) is shown with a black bar. Symbol descriptions follow Fig. S2.

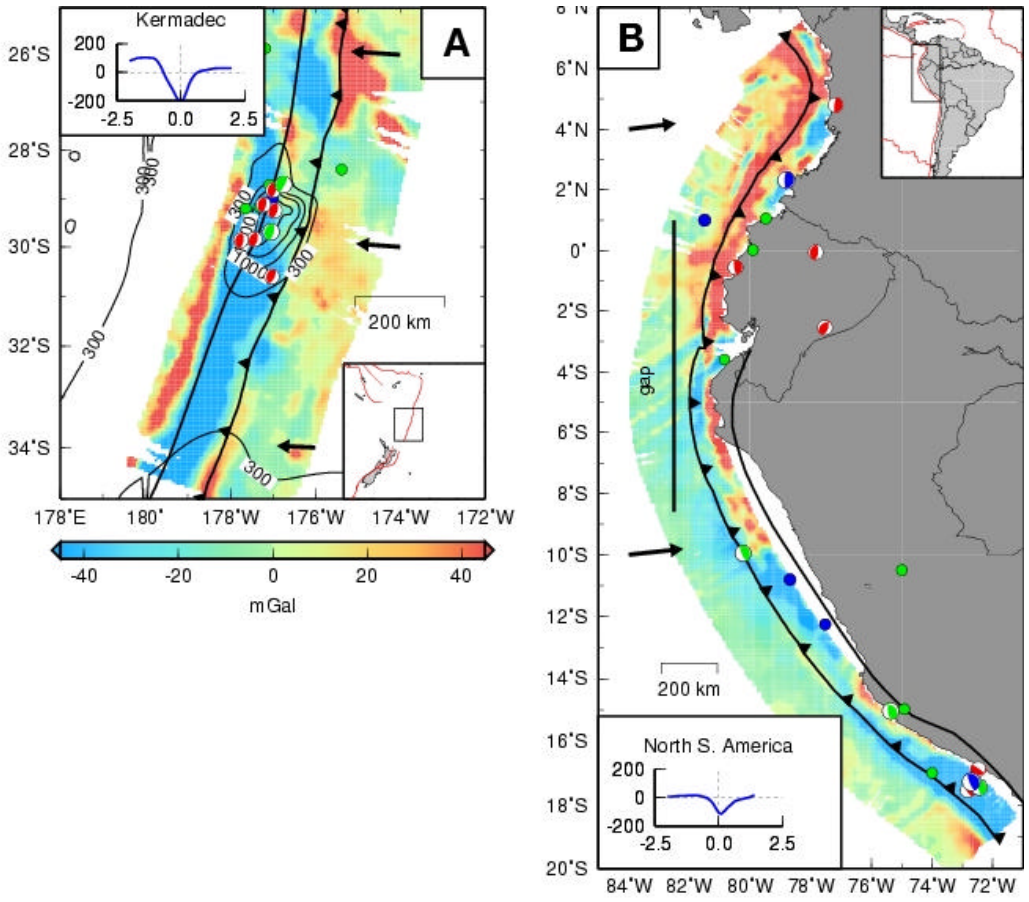

References for Supporting OnlineMaterial

S1. T. Lay, T. Wallace, in *Modern Global Seismology,* 521p (1995).

S2. H. Kanamori, D. L. Anderson, *Bull. Seis. Soc. Am.* **65**, 1073-1095 (1975).

S3. P. Chen, H. Chen, *Tectonophysics* **166**, 53-72 (1989).

S4. H. Kanamori, *Tectonophysics* **93**, 185-199 (1983).

S5. L. Ruff, H. Kanamori, *Phys. Earth Planet. Inter.* **31**, 202 (1983).

S6. S. E. Barrientos, S. N. Ward, *Geophys. J. Int.* **103**, 589 (1990).

S7. J. M. Johnson, K. Satake, *Pure Apply. Geophysics.* **154**, 541 (1999).

S8. National Geophysical Data Center, ETOPO-5 bathymetry/topography data, *Data Announc.* 88-MCG-02, Natl. Oceanic and Atmos. Admin. U. S Dep. Commer., Boulder, Colo. (1988).

S9. W. H. F. Smith, *J. Geophys. Res.* **98**, 9591 (1993).

S10. E. L. Lehmann, in *Testing Statistical Hypothesis.* Wiley publication in statistics, 369 pp (1959).

S11. National Geophysical Data Center, Global Relief data (CD-ROM). World data center for marine geology and geophysics, Boulder, Colo. (1993)

S12. O. Gudmundsson, M. Sambridge, *J. Geophys. Res*. **103**, 7121 (1998).

S13. C. DeMets, R. G. Gordon, D. F. Argus, *Geophys. Res. Lett.* **21**, 2191 (1994).

S14. S. E. Barrientos, S. N. Ward, *Geophys. J. Int.* **103**, 589 (1990).

S15. T. Lay, H. Kanamori, L. Ruff, *Earthquake Pred. Res.* **1**, 1 (1982).

S16. J. M. Johnson, K. Satake, *Pure Apply. Geophysics.* **154**, 541 (1999).

S17. L. Ruff, H. Kanamori, *Phys. Earth Planet. Inter.* **31**, 202 (1983).

S18.National Geophysical Data Center, Total Sediment Thickness of the World's Oceans & Marginal Seas, Natl. Oceanic and Atmos. Admin. U. S Dep. Commer., Boulder, Colo. (1996).